Available online at www.sciencedirect.com
ScienceDirect
Journal of Nuclear Materials 361 (2007) 192–205
journal of nuclear materials
www.elsevier.com/locate/jnucmat

Fracture mechanism maps in unirradiated and irradiated metals and alloys

Meimei Li *, S.J. Zinkle

Materials Science and Technology Division, Oak Ridge National Laboratory, P.O. Box 2008, MS 6138, Oak Ridge, TN 37831, United States

Abstract

This paper presents a methodology for computing a fracture mechanism map in two-dimensional space of tensile stress and temperature using physically-based constitutive equations. Four principal fracture mechanisms were considered: cleavage fracture, low temperature ductile fracture, transgranular creep fracture, and intergranular creep fracture. The methodology was applied to calculate fracture mechanism maps for several selected reactor materials, CuCrZr, 316 type stainless steel, F82H ferritic–martensitic steel, V4Cr4Ti and Mo. The calculated fracture maps are in good agreement with empirical maps obtained from experimental observations. The fracture mechanism maps of unirradiated metals and alloys were modified to include radiation hardening effects on cleavage fracture and high temperature helium embrittlement. Future refinement of fracture mechanism maps is discussed.

1. Introduction

The deformation and fracture behavior of metals and alloys can be significantly modified by neutron irradiation. Professor Monroe S. Wechsler has made significant contributions to our understanding of deformation and fracture mechanisms in irradiated metals and alloys. As reviewed in his seminal paper on dislocation channeling [1], plastic deformation in irradiated metals and alloys can be quite inhomogeneous as opposed to uniform deformation that occurs in annealed materials. Irradiation-induced defect clusters such as black dots, dislocation loops, and stacking fault tetrahedra can be removed by glide dislocations, resulting in the formation of cleared channels (dislocation channels). Dislocation channeling is observed in a number of irradiated face-centered cubic (fcc), body-centered cubic (bcc) and hexagonal close-packed (hcp) metals and alloys during mechanical testing. The phenomenon of dislocation channeling has led to the recognition that this inhomogeneous deformation may play a significant role in radiation embrittlement, plastic instability, and radiation-assisted stress corrosion cracking.

The fracture issues in irradiated metals and alloys, particularly at low temperatures were also thoroughly reviewed by Wechsler [2]. The phenomenon of 'radiation embrittlement' in ductile metals (loss of uniform elongation) is characterized by the premature onset of plastic instability at low

* Corresponding author. Tel.: +1 865 5761813; fax: +1 865 2413650.
E-mail address: lim1@ornl.gov (M. Li).

0022-3115/$ - see front matter © 2007 Elsevier B.V. All rights reserved.
doi:10.1016/j.jnucmat.2006.12.017

tensile elongation values, and dislocation channeling seems to be largely responsible for the dramatic ductility loss. Metals that experience distinct ductile-to-brittle transition temperatures (DBTT) associated with a transition from cleavage to ductile fracture can experience radiation embrittlement with an increased DBTT following irradiation. Wechsler [2] also pointed out that radiation embrittlement is likely associated with changes in plastic properties particularly with inhomogeneous plastic deformation rather than changes in inherent fracture processes.

The understanding of deformation and fracture behavior of irradiated materials requires a knowledge of deformation and fracture mechanisms in unirradiated conditions. It is well-recognized that Ashby-type deformation mechanism maps [3–6] can provide an overview of the deformation behavior of a material in response to stress and temperature. Deformation mechanism maps describe the dominant deformation mode at a given temperature, stress or strain rate condition. They are constructed by physically-based constitutive equations for various operative deformation mechanisms in the shear modulus-normalized stress and the melting point normalized-temperature coordinates. The maps provide useful guidance in identifying deformation mechanisms, defining operating conditions and developing new alloys. Our previous work has also shown that the deformation behavior of irradiated metals can be conveniently represented by irradiation-modified Ashby deformation mechanism maps [5,6]. Radiation hardening and radiation-enhanced softening can be incorporated into deformation maps by modifying the dislocation glide flow stress and the dislocation creep frictional stress. Dislocation channeling can be considered as a specialized case of the normal dislocation glide deformation mechanism. Irradiation creep represents a new deformation mechanism, whereas helium embrittlement at high temperature may be considered similar to diffusional creep [5]. With the success of 'deformation mechanism maps', it is worthwhile to examine how fracture mechanisms may be quantified in a similar convenient map formulation.

The idea of 'fracture mechanism maps' was first proposed by Wray [7] in 1969 and studied in detail by Ashby et al. [8–12]. Ashby et al. developed a methodology to construct fracture mechanism maps and plotted the maps for a number of fcc and bcc metals. Unlike deformation mechanism maps that were computed from model-based constitutive equations, these fracture mechanism maps were generated based on experimental observations. The maps were constructed by compiling experimental data and drawing field boundaries that bound blocks of data having a given fracture mode. Few attempts have been made in the past to calculate the fracture mechanism maps using mechanistically-derived constitutive equations [13,14]. The difficulties of doing so are primarily due to the fact that the model-based constitutive equations for fracture mechanisms are not well-established. The construction of fracture mechanism maps is also complicated by stress state, notch effects, deformation rate, mechanical constraint, etc.

The fracture behavior of irradiated metals and alloys is not well understood from a mechanistic viewpoint. The problem stems from complexity of fracture in unirradiated materials and irradiation-induced changes in many intrinsic and extrinsic properties that confound the complex situation. However, it is clearly valuable for irradiation-modified fracture behavior to be modeled on a physical basis, and the fracture behavior of irradiated materials thereby predicted on a constitutive level.

In this paper, we explore the physical models for several common fracture mechanisms, and apply the model-based constitutive equations to compute the fracture mechanism maps for selected nuclear reactor materials such as CuCrZr (Cu–0.8wt%Cr–0.1wt%Zr), 316 type stainless steel, V4Cr4Ti (V–4wt%Cr–4wt%Ti), F82H (Fe–8wt%Cr–2wt%WVTa) ferritic–martensitic steel and pure Mo. We also attempt to include the impact of radiation effects in fracture mechanism maps with the emphasis on low temperature cleavage fracture and high temperature intergranular creep due to helium embrittlement.

2. Fracture mechanisms and physical models

In the present work we focus on the fracture of fcc and bcc metals and alloys. For the purpose of constructing fracture mechanism maps, seven fracture mechanisms have been distinguished, i.e. fracture at the ideal strength, low temperature brittle fracture (cleavage), low temperature ductile fracture, high temperature transgranular creep fracture, high temperature intergranular creep fracture, rupture and dynamic fracture [9,10]. Only the first five fracture mechanisms are considered here, and their physical models are discussed below.

2.1. Fracture at the ideal strength

The theoretical cohesive strength of a material, σ_{ideal} is given as [9]:

$$\sigma_{ideal} \approx \frac{E(T)}{10}, \tag{1}$$

where $E(T)$ is the temperature-dependent Young's modulus. It defines the upper limit of the material strength.

2.2. Low temperature brittle fracture – cleavage

Cleavage fracture is a brittle transgranular fracture that occurs through cleaving of crystals along well-defined crystallographic planes. It is often seen in bcc metals and alloys at low temperatures. Cleavage is rarely seen in fcc metals.

The origin of the cleavage fracture is still not clear. The general proposition is that cleavage crack nucleation is always preceded by some plastic deformation. Various mechanisms for crack nucleation have been suggested, including dislocation pile-up at grain boundaries or intersections of dislocations. Zener [15] suggested that the stress level at the head of a dislocation pile-up at a grain boundary could be sufficient to nucleate a crack. Stroh [16] developed this idea by deriving a fracture criterion from the elastic strain energy of a dislocation pile-up. The critical condition for crack nucleation at the end of a dislocation pile-up was defined as

$$\sigma_{cleave} = 3.06 \cdot \sqrt{\frac{12\mu(T)\gamma}{\pi(1-\nu)L}}, \tag{2}$$

where γ is the surface energy, ν the Poisson's ratio, $\mu(T)$ the temperature-dependent shear modulus, and L the slip band half-length, which is approximately one-half the grain diameter (all nomenclature for this paper is summarized in Table 1). With this mechanism, crack nucleation is predicted to be the most difficult stage during the fracture process, and cleavage fracture is therefore nucleation-controlled [17].

Cottrell proposed an alternative dislocation mechanism for nucleating a cleavage microcrack, specifically for bcc metals [18]. It was suggested that dislocations moving on two intersecting {101} planes interact to form a sessile dislocation whose Burgers vector ⟨001⟩ is normal to the cleavage plane. The coalescence of a number of these sessile

Table 1
Symbols and definitions

α	Forest hardening strength constant
δ	Grain boundary thickness (m)
ε	Tensile strain
$\dot{\varepsilon}$	Strain rate (s^{-1})
$\dot{\varepsilon}_p$	Pre-exponential constant (lattice resistance controlled plasticity) (s^{-1})
$\dot{\varepsilon}_0$	Pre-exponential constant (obstacle-controlled plasticity) (s^{-1})
$\dot{\varepsilon}_{ss}$	Minimum creep rate (s^{-1})
ε_c	Critical strain for onset of cavitation
ε_f	Fracture strain
ε_N	Strain required for void nucleation
ε_G	Strain required for void growth
ε_u	Uniform elongation
σ	Tensile stress (N/m^2)
σ_c	Critical stress (N/m^2)
σ_{uts}	Ultimate tensile strength (N/m^2)
σ_{PIS}	Plastic instability stress (N/m^2)
σ_{FS}	True fracture stress (N/m^2)
σ_m	Mean stress (N/m^2)
σ_{cleave}	Cleavage fracture stress (N/m^2)
σ_{void}	Void nucleation stress (N/m^2)
σ_{ideal}	Theoretical cohesive strength (N/m^2)
σ_0	Orowan stress (N/m^2)
γ	Surface tension (J/m^2)
τ	Shear stress (N/m^2)
τ_2	Dislocation friction stress (dislocation creep) (N/m^2)
τ_0	Flow strength for obstacle cutting at 0 K (N/m^2)
τ_p	Lattice resistance of Peierls stress at 0 K (N/m^2)
μ_0	Shear modulus at 300 K (N/m^2)
$\mu(T)$	Temperature-dependent shear modulus (N/m^2)
ν	Poisson's ratio
Ω	Atomic volume (m^3)
ΔF	Helmholz free energy (J/mol)
a	Grain boundary void spacing (m)
b	Burgers vector (m)
c	Crack length (m)
d	Grain size (m)
f_v	Volume fraction of particles
k	Boltzmann's constant
k_y^s	Hall–Petch yielding constant
n	Dislocation power-law creep exponent
p	Work of plastic deformation per unit increase in the area of the crack (J/m^2)
r	Particle radius/helium bubble radius (m)
r_0	Initial helium bubble radius (m)
t	Time (s)
t_r	Rupture time (s)
A	Power-law creep constant
B	Grain boundary cavitation constant (Hull–Rimmer equation)
C_{MG}	Monkman–Grant constant
D_{gb}	Grain boundary diffusion coefficient (m^2/s)
D_c	Dislocation core diffusion coefficient (m^2/s)
D_{SD}	Lattice diffusion coefficient (m^2/s)
E_0	Young's modulus at 300 K
$E(T)$	Temperature-dependent Young's modulus (N/m^2)
L	Slip band half-length (m)

Table 1 (*continued*)

P	Gas pressure (N/m^2)
R	Average radius of the void (m)
R_f	Final void radius (m)
R_i	Initial void radius (m)
RA	Reduction in area
T	Temperature (K)
T_m	Melting point (K)

dislocations forms a wedge-shaped crack. The cleavage fracture stress is therefore given by

$$\sigma_f = \frac{2\mu(T)\gamma}{k_y^s\sqrt{d}}, \tag{3}$$

where k_y^s is the Hall–Petch yielding constant, and d is the grain size.

The propagation of an existing cleavage microcrack can be modeled by a modified Griffith's theory to take into account plastic deformation during crack propagation, i.e. [19]:

$$\sigma = \sqrt{\frac{2E(p+\gamma)}{\pi c}}, \tag{4}$$

where c is the crack length, and p is the work of plastic deformation per unit increase in the area of the crack.

2.3. Low temperature ductile fracture

The most common ductile fracture mode at low temperatures (below $\sim 0.3T_m$) in metals and alloys is transgranular fracture by void nucleation, growth and coalescence. Voids nucleate at inclusions or second phase particles during plastic deformation. Further straining causes the voids to grow until they link together to produce ductile fracture. Void nucleation at particles can occur by two mechanisms: (1) decohesion of the particle–matrix interface, or (2) by fracture of the particle. There have been many attempts to model void nucleation by decohesion of the particle–matrix interface. All the models have the same premise that the stress at the interface must exceed some critical level before void nucleation occurs. The differences between the models primarily reside in how the energy criterion is treated. Here, we present an example of such models proposed by Goods and Brown [20]. The flow stress for void nucleation by decohesion is given by the following equation:

$$\sigma_{void} = 3.06\left(\sigma_0 + \alpha f_v^{1/2}\left(\frac{\varepsilon_c b}{r}\right)^{1/2}\cdot\mu(T) + 5.4\alpha f_v\left(\frac{\varepsilon_c b}{r}\right)^{1/2}\cdot\mu(T)\right), \tag{5}$$

where σ_0 is the Orowan stress, α is a constant related to forest hardening strength [21], b the Burgers vector, f_v the volume fraction of particles, r the particle radius, and ε_c the critical strain for onset of cavitations. The nucleation strain, ε_N is, accordingly, given by

$$\varepsilon_N \geqslant 1.7\frac{r}{b}\left(\frac{\sigma_{void}-3\sigma_0}{\mu(T)}\right)^2\left(1+3f_v+\frac{f_v^{0.5}}{1.8}\right)^{-2}. \tag{6}$$

Void growth has been modeled using continuum mechanics approaches. Rice and Tracy [22] derived an equation that is applied for the growth of an initially spherical void:

$$\frac{dR}{R} = 0.32\exp\left(1.5\frac{\sigma_m}{\sigma}\right)d\varepsilon, \tag{7}$$

where R is the average radius of the void, σ_m the mean stress. The strain that is required for void growth, ε_G is given by

$$\varepsilon_G = \ln\left(\frac{R_f}{R_i}\right)\frac{1}{0.32\exp\left(1.5\frac{\sigma_m}{\sigma}\right)}, \tag{8}$$

where R_f and R_i are the final and initial void radii, respectively. This model works reasonably well at small strains for materials containing a small volume fraction of inclusions.

Void coalescence can be treated by the plastic limit-load model proposed by Thomason [23–25]. Void coalescence occurs by internal microscopic necking of the intervoid matrix when the plastic limit-load stress is exceeded.

In spite of a vast amount of research on modeling ductile fracture, current understanding of the physical process of void nucleation, growth and linkage is inadequate to mechanistically model critical stresses and tensile ductility. In this paper, a constitutive stress–strain model is used for determining the critical stresses of ductile fracture. More discussion is given in Section 3.

2.4. Transgranular creep fracture

At temperatures above 0.3–$0.5T_m$, metals and alloys deform by a time-dependent process, creep. At a relatively low temperature and high stress, dislocation creep by lattice diffusion or dislocation core

diffusion is a dominant deformation mechanism. The strain rate has a power-law relationship with the applied stress, and is described by [5]:

$$\dot{\varepsilon}_{ss} = \frac{A\mu b}{kT}\left\{D_{SD} + 200D_c\left(\frac{\tau-\tau_2}{\mu}\right)^2\right\}\left(\frac{\tau-\tau_2}{\mu}\right)^n \tau \geqslant \tau_2, \tag{9}$$

where the dimensionless constant $A = 10^9$, the power law exponent n is usually 5, and τ_2 the dislocation friction stress associated with solute or other dislocation obstacles, D_{SD} and D_c are the lattice diffusion coefficient and dislocation core diffusion coefficient, respectively, and T is the absolute temperature. For this deformation mechanism, materials fail in a ductile transgranular manner, which resembles low temperature ductile fracture but is controlled by diffusion-assisted void growth within the grains. The rupture time can be described by the Monkman–Grant relation [26]:

$$t_r\dot{\varepsilon}_{ss} = C_{MG}, \tag{10}$$

where t_r is the rupture time, $\dot{\varepsilon}_{ss}$ the minimum creep rate, and C_{MG} is a constant.

2.5. Intergranular creep fracture

At higher temperature, the fracture mode often changes from transgranular creep fracture to intergranular creep fracture. Intergranular creep fracture can occur at high stresses by the nucleation and growth of wedge cracks formed at triple-points of grain boundaries due to grain boundary sliding, or at low stresses by the nucleation and growth of grain boundary cavities. Here, we discuss only grain boundary cavitation.

There are several mechanisms to nucleate voids at grain boundaries. Impurity particles present at grain boundaries may nucleate cavities due to lack of cohesion with the lattice. Cavities may also nucleate at the intersection of slip bands and grain boundaries due to a dislocation pile-up. Once nucleated, voids will grow by vacancy diffusion and condensation when the applied stress is sufficiently large to overcome the tendency for the void to shrink by surface tension. With the assumption that the cavity growth is controlled by grain boundary diffusion of vacancies and the driving force of void growth is the gradient of chemical potential at grain boundaries, Hull and Rimmer derived the void growth rate given by the following equation [27]:

$$\frac{dR}{dt} = \frac{\delta D_{gb}\Omega}{2kTR}\frac{\sigma}{a}. \tag{11}$$

The rupture time can be estimated by integrating Eq. (11) from R_i to $a/2$ and assuming that $R_i \ll a/2$:

$$t_r = B\cdot\frac{kTa^3}{(D_{gb}\delta)\sigma\Omega}, \tag{12}$$

where R is the radius of voids, R_i the initial radius of voids, a the mean void spacing, σ the uniaxial stress, k the Boltzmann's constant, 13.8×10^{-24} J/K, T the absolute temperature, D_{gb} the grain boundary diffusion coefficient, δ the grain boundary thickness, Ω the atomic volume, and B is a constant depending on spatial distribution of voids, varying from 0.006 to 0.05.

The Hull–Rimmer model has been modified by several researchers. Speight and Harris [28] refined the Hull–Rimmer equation by assuming that the grain boundary cavity concentration increases at a constant rate, and the void growth rate is expressed as

$$\frac{dR}{dt} = \frac{\delta D_{gb}\Omega}{2kTR}\frac{\left(\sigma-\frac{2\gamma}{R}\right)\left(\frac{1}{R}-\frac{4R}{a^2}\right)}{\left[\ln\left(\frac{a}{2R}\right)-\frac{\left(a^2-4R^2\right)}{2a^2}\right]}, \tag{13}$$

where γ is the surface tension of the void.

A further modification to include constrained cavity growth was initially made by Dyson [29,30]. It was suggested that cavities at grain boundaries grow by diffusion, while surrounding grains deform by power-law creep to accommodate cavity growth. A model for this coupled diffusion and power-law creep cavity growth was proposed by Edward and Ashby. Details are described in Ref. [31].

3. Construction of fracture mechanism maps

3.1. Methodology for constructing fracture mechanism maps

Metals and alloys may fail by one of several competing mechanisms. The dominant mechanism depends on external parameters such as temperature and stress, and on internal material parameters. The dominance of each fracture mechanism can be demonstrated in a fracture mechanism map. Each fracture mechanism may be described by a constitutive equation that relates external variables of stress, temperature, and fracture strain or time to fracture, and internal material properties. The general form

of the constitutive equation for a fracture mechanism is given by

$$\begin{aligned} \varepsilon_f &= f(\sigma, T, S_i) \text{ or,} \\ t_f &= f(\sigma, T, S_i), \end{aligned} \tag{14}$$

where ε_f is the fracture strain, t_f the rupture time, σ the applied stress, T the temperature, and S_i are a set of material properties such as lattice parameter, modulus, surface energy, etc.

In this paper we selected the suitable physical models for several discrete fracture mechanisms, and calculated mechanism fields in fracture maps using the model-based constitutive equations. The equations are summarized in Fig. 1, which also shows a generic fracture mechanism map. Below the field of fracture at the ideal strength, the field labeled as 'dynamic fracture' describes fast fracture at a very high strain rate that occurs at high stresses [9]. Under the 'dynamic fracture' field, the high stress regime where plasticity is a dominant deformation mode is divided into cleavage fracture and ductile fracture fields. The transition of fracture modes is determined by comparing the flow stress and the cleavage fracture stress. When the flow stress is higher than the fracture stress, cleavage fracture is dominant; when the flow stress is smaller than the fracture stress, ductile fracture is prevalent. As shown in Fig. 1, the cleavage fracture stress was determined by the Zener–Stroh crack nucleation model (Eq. (2)), and the flow stress was determined by the constitutive equations for dislocation glide [4], i.e.

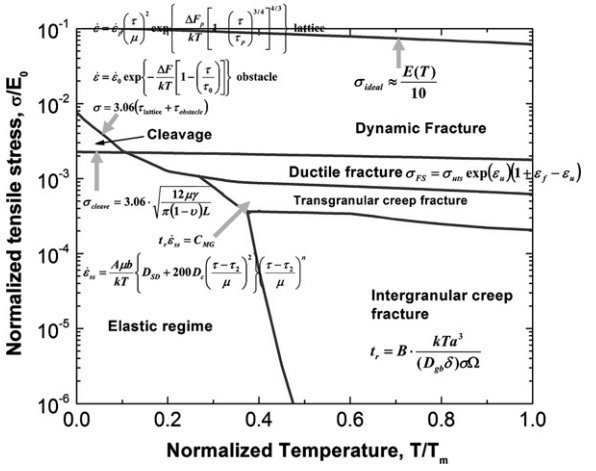

Fig. 1. Overview of a fracture mechanism map.

$$\begin{aligned} \dot{\varepsilon} &= \dot{\varepsilon}_p \left(\frac{\tau}{\mu}\right)^2 \exp\left\{-\frac{\Delta F_p}{kT}\left[1-\left(\frac{\tau}{\tau_p}\right)^{3/4}\right]^{4/3}\right\} \text{ lattice,} \\ \dot{\varepsilon} &= \dot{\varepsilon}_0 \exp\left\{-\frac{\Delta F}{kT}\left[1-\left(\frac{\tau}{\tau_0}\right)\right]\right\} \text{ obstacle,} \\ \sigma &= 3.06(\tau_{\text{lattice}} + \tau_{\text{obstacle}}). \end{aligned} \tag{15}$$

The flow stress is sensitive to the strain rate, particularly for bcc metals and alloys. A strain rate of $1 \times 10^{-3}\ s^{-1}$ was assumed in the calculation. The ductile fracture field is bounded by the critical stress for void nucleation and by the true fracture stress calculated using a constitutive stress–strain model. Since void nucleation usually occurs prior to necking, as reported in many experiments [20,32,33], the lower boundary of the ductile fracture field was described by the true ultimate tensile stress, which is also called plastic instability stress (PIS), σ_{PIS}. The upper boundary was determined by the true fracture stress, σ_{FS} that was calculated using a linear hardening rate equation for necking [19,34]:

$$\begin{aligned} \sigma_{PIS} &= \sigma_{uts} \exp(\varepsilon_u), \\ \sigma_{FS} &= \sigma_{PIS}(1 + \varepsilon_f - \varepsilon_u), \quad \varepsilon_f = \ln\frac{1}{1-RA}, \end{aligned} \tag{16}$$

where σ_{uts} is the ultimate tensile strength, ε_u the uniform elongation, ε_f the true fracture strain and RA is the reduction in area.

In the high temperature and low stress regime where creep is significant, two fracture mechanisms were considered: transgranular creep fracture and intergranular creep fracture. The failure boundaries of transgranular creep damage were calculated by the coupled equations of the dislocation creep constitutive law (Eq. (9)) and the Monkman–Grant relation (Eq. (10)). The field of intergranular creep fracture was determined by the Hull–Rimmer model of grain boundary void growth rate (Eq. (12)).

The fracture mechanism maps are presented in a stress-temperature space. The tensile stress was selected as a critical parameter. The ordinate is the tensile stress normalized by the Young's modulus at 20 °C, σ/E_0, and the abscissa is the temperature normalized by the melting point, i.e. the homologous temperature, T/T_m. The predominant fracture mechanism in different regimes of stress and temperature is determined by the mode that requires the least level of stresses, and the field boundaries are the loci of points at which two mechanisms have equivalent failure strengths. Superimposed are the

contours of constant time-to-fracture or strain-to-fracture.

3.2. Fracture mechanism maps for unirradiated metals and alloys

The fracture mechanism maps for several nuclear reactor materials, CuCrZr, 316 SS, V4Cr4Ti, Mo and F82H are shown in Figs. 2–6. The material parameters used in the construction of the maps are listed in Table 2. The data were taken from previous work on the construction of deformation and fracture mechanism maps [4,5,9,10].

Fig. 2 is the calculated fracture mechanism map for solution annealed and aged CuCrZr. The ductile fracture field was determined by the temperature dependence of plastic instability stress (true ultimate

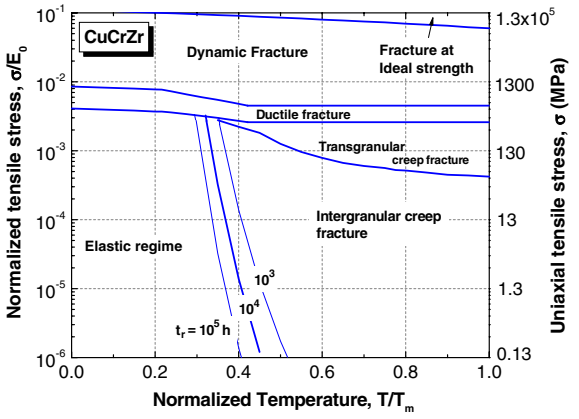

Fig. 2. Calculated fracture mechanism map for CuCrZr (grain size of 30 μm).

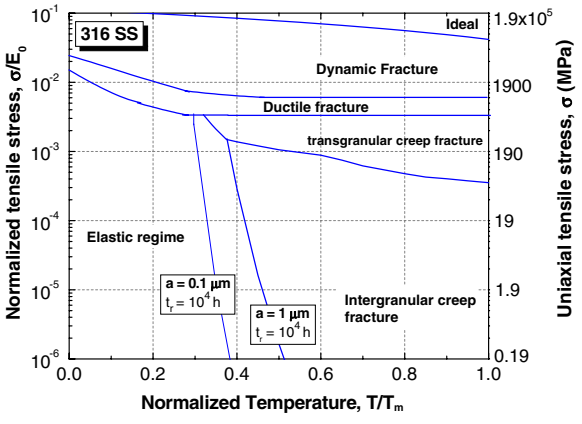

Fig. 3. Calculated fracture mechanism map for 316 SS (grain size of 50 μm).

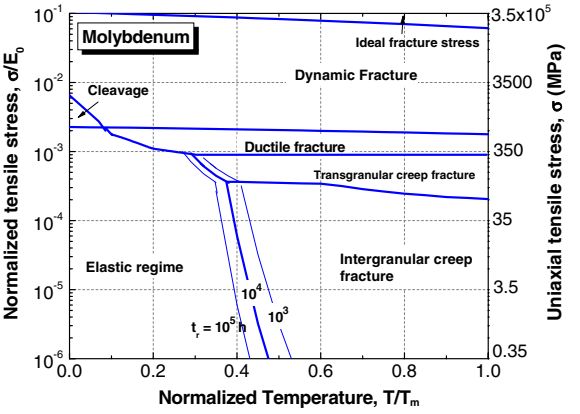

Fig. 4. Calculated fracture mechanism map for Mo (grain size of 70 μm).

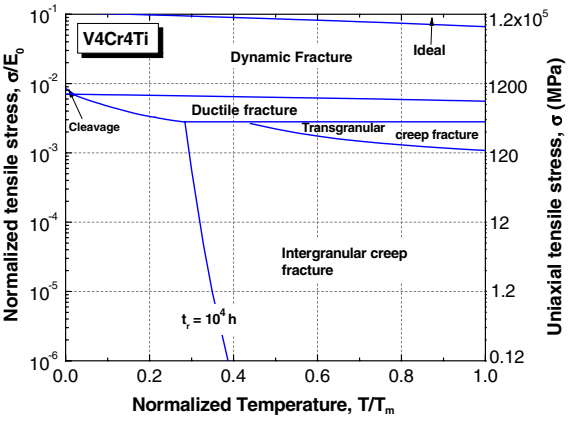

Fig. 5. Calculated fracture mechanism map for V4Cr4Ti (grain size of 20 μm).

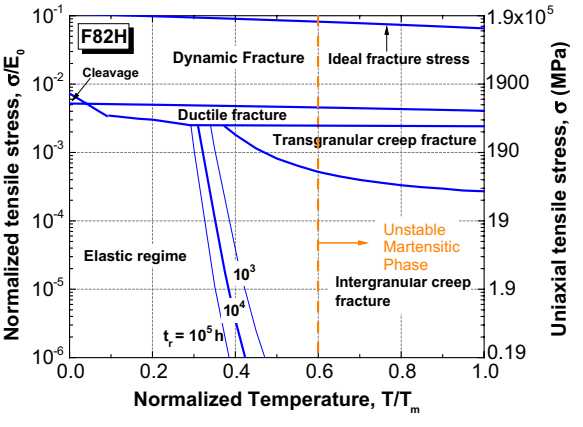

Fig. 6. Calculated fracture mechanism map for F82H ferritic–martensitic steel (grain size of 22 μm).

Table 2
Material parameters for CuCrZr, 316 SS, Mo, V4Cr4Ti and F82H

Parameter	CuCrZr	316 SS	Mo	V4Cr4Ti	F82H
T_M (K)	1358	1672	2883	2163	1800
b (nm)	0.256	0.258	0.273	0.262	0.248
Ω (m^3)	1.18×10^{-29}	1.21×10^{-29}	1.58×10^{-29}	1.38×10^{-29}	1.38×10^{-29}
E_0 (GPa)	129	192	349	123	219
$(d\mu/dT)/\mu_0$ (10^{-4} K^{-1})	−3.8	−3.9	−1.5	−1.7	−2.3
D_0^{SD} (m^2/s)	0.6×10^{-4}	0.4×10^{-4}	5.0×10^{-5}	0.3×10^{-4}	1.0×10^{-4}
Q_{SD} (kJ/mol)	200	280	405	300	260
δD_0^{gb} (m^3/s)	5.0×10^{-15}	0.1×10^{-13}	5.5×10^{-14}	1.0×10^{-13}	1.0×10^{-13}
Q_{gb} (kJ/mol)	104	150	263	160	150
D_0^c (m^2/s)	0.4×10^{-4}	0.1×10^{-4}	3.4×10^{-4}	0.1×10^{-4}	0.1×10^{-4}
Q_c (kJ/mol)	148	190	263	230	210
n	5	5	4.85	5	5
τ_2 (MPa)	15	15	15	15	20
B	0.05	0.05	0.05	0.05	0.05
a (μm)	1	1, 0.1	1	1	1
γ (J/m^2)	2.2	2.7	2.9	3.0	2.7

tensile strength) and true fracture stress that was calculated from the tensile properties [35–37]. In the temperature range where tensile property data are not available, the temperature-dependence of stresses is assumed to be the same as that of the shear modulus. Five mechanism fields are shown in the map: fracture at the ideal strength, dynamic fracture, ductile fracture, transgranular creep fracture, and intergranular creep fracture. At low temperatures and high stresses, the alloy fails by ductile transgranular fracture. When the alloy fails in the ductile mode, the fracture surface shows dimpled rupture (on a microscopic scale) by microvoid coalescence. As temperature increases, the material starts to creep and fails either by transgranular creep fracture or by intergranular creep fracture. At high stresses the alloy tends to fail in a transgranular mode by void nucleation, growth and coalescence. The appearance of the fracture surface resembles low temperature ductile fracture. However, the deformation mode that causes failure has changed from low temperature dislocation glide to high temperature dislocation creep. The change in deformation mechanism affects the local stress for void nucleation and the condition for void growth and linkage. Void growth is assisted by diffusion in the creep regime, while void growth is a plasticity-dominated process at low temperature [20]. Below the transgranular creep fracture field lies a field of intergranular creep fracture. The intergranular creep fracture is a dominant mechanism over a wide range of temperatures at lower stresses. The alloy fails from void nucleation and growth along grain boundaries due to stress-directed vacancy diffusion. In all the calculated maps the void spacing was assumed to be 1 μm. Fig. 2 also shows contours of three different rupture times varying from 1000 to 100 000 h. The field of intergranular creep fracture expands as the rupture time increases, indicating that intergranular creep fracture will occur at a lower temperature in a prolonged creep rupture test.

The calculated fracture mechanism map for 316 SS is shown in Fig. 3. The tensile property data used to determine the ductile fracture regime were taken from several sources [38–44]. Note that both CuCrZr and 316 SS have fcc crystal structure, and their maps show similar features and both have five primary fracture mechanism fields. It is noted that the temperature dependence of ductile fracture field boundaries is much deeper than that for CuCrZr. This is due to the strong temperature dependence of its tensile properties, particularly the ultimate tensile strength of 316 SS at low temperatures. It is known that most austenitic stainless steels are metastable at low temperatures. Austenitic stainless steels such as 316 SS tend to undergo stress-induced martensitic phase transformation at cryogenic temperatures, resulting in enhanced tensile strength. Tensile elongation and reduction in area decreases with decreasing temperature, but generally are still above 50%, and the fracture surfaces of 316 SS tested at 4 K showed dimpled ductile fracture mode [41,45,46]. Fig. 3 also shows the effect of variation of the mean spacing of grain boundary voids on intergranular fracture mode at high temperatures. At a

rupture time of 10 000 h, a 316 SS alloy with a larger spacing of voids (1 μm) experiences intergranular creep fracture at a higher temperature ($\Delta T/T_m \sim 0.1$ at a normalized stress of 10^{-5}) than the alloy with a smaller void spacing (0.1 μm).

Fig. 4 shows the calculated fracture mechanism map for pure Mo with a grain size of 70 μm. The tensile data were taken from several studies [47–50]. As the true fracture stress for ductile fracture is higher than the cleavage stress, the upper boundary of the ductile fracture field was defined by the cleavage fracture stress. The map for Mo typifies those for the bcc metals. It shows six basic mechanism fields: fracture at the ideal strength, dynamic fracture, cleavage, low temperature ductile fracture, transgranular creep fracture and intergranular creep fracture. Compared to fcc metals and alloys, the presence of the cleavage fracture regime in bcc metals is a new feature. It occurs at temperatures below $\sim 0.09T_m$ (−12 °C) in Mo. The calculated cleavage regime represents only the nucleation-controlled mechanism for a material without pre-existing flaws (e.g. un-notched tensile deformation in high-purity Mo). As the temperature is increased, the yield stress decreases rapidly and plastic flow precedes fracture, leading to ductile fracture. As temperature increases to $0.3T_m$, creep deformation becomes significant. The material fails in a transgranular fracture mode at higher stresses, and exhibits intergranular creep fracture at lower stresses ($\sigma < 130$ MPa) and higher temperatures.

The calculated fracture mechanism map for a bcc alloy, V4Cr4Ti is shown in Fig. 5. A grain size of 20 μm was assumed in the calculation. The true fracture stress of low temperature ductile fracture was calculated from tensile property data [51–56]. Again, the upper boundary of ductile fracture is determined by the cleavage stress, which is lower than the true ductile fracture stress, as with Mo. The map, similar to the Mo fracture map, shows six principal mechanism fields. Compared to pure Mo, V4Cr4Ti shows a much smaller cleavage fracture field, in agreement with experimental observations on vanadium versus molybdenum alloys [49]. The transition temperature from cleavage fracture to ductile fracture is about $0.02T_m$ (−230 °C) for V4Cr4Ti, while the transition temperature is about $0.09T_m$ (−12 °C) for Mo. V4Cr4Ti is also more susceptible to creep fracture than pure Mo. The creep fracture occurs at a higher stress level in V4Cr4Ti than in Mo.

Fig. 6 shows the calculated fracture mechanism map for another bcc alloy, F82H. F82H is an example of reduced-activation ferritic–martensitic steel, one of the most promising structural materials for nuclear reactor applications. The material parameters used in the map calculation are listed in Table 2. A grain size of 22 μm was assumed in the calculation. The tensile property data of F82H were taken from several sources [57–59]. It should be mentioned that the fracture mechanism map of F82H should be used with caution at temperatures above $\sim 0.6T_m$, where the parameters used in the calculation may not be valid due to the unstable martensitic phase.

4. Modification of fracture mechanism maps by irradiation

Neutron irradiation significantly modifies the deformation behavior of metals and alloys. The effects include radiation hardening, radiation-enhanced softening, radiation creep and high temperature helium embrittlement, etc. [5]. The fracture behavior of materials can also be significantly altered by neutron irradiation, but the effects are more complicated and less understood than the deformation behavior. Fracture mechanisms in irradiated austenitic stainless steels were reviewed by Grossbeck in 1977 [60], and a schematic fracture mechanism map was presented for austenitic stainless steels after irradiation to high neutron fluences. Three major effects of radiation on fracture behavior were addressed, i.e. low temperature fracture modified by radiation hardening, helium embrittlement at high temperatures, and 'channel fracture'. Our focus here is on the radiation hardening-enhanced cleavage and the high temperature intergranular fracture by helium embrittlement.

4.1. Cleavage fracture

Due to the formation of a high number density of defect clusters during irradiation at low temperatures (below $\sim 0.3T_m$), the matrix strength of a material is significantly increased through the interactions of dislocations with defect clusters. For bcc metals and alloys, the increase in flow stress raises the upper bound of cleavage fracture regime, while the cleavage fracture stress is assumed to remain unchanged. Therefore cleavage fracture is favored over a wider temperature range following low temperature irradiation. The insensitivity of the cleavage fracture stress to neutron irradiation can be understood from the Zener–Stroh dislocation

pile-up model, where key parameters that determine the fracture stress are considered not to be readily affected by radiation damage. Experimental studies on the fracture stress in fcc and bcc metals and alloys such as austenitic stainless steels have also shown that the fracture stress is nearly unchanged following irradiation [56,61–65]. The expansion of the cleavage fracture regime by radiation hardening can be modeled by the following equation:

$$\sigma = \sigma^{\text{unirr}} + \Delta\sigma_{\text{ys}}^{\text{irr}}(T), \tag{17}$$

where $\Delta\sigma_{\text{ys}}^{\text{irr}}$ is the increase in yield stress after irradiation.

4.2. Helium embrittlement at high temperatures

Helium gas is produced by nuclear transmutation during irradiation and tends to precipitate into bubbles at elevated temperatures due to its low solubility in metals. If helium bubbles are formed in the matrix, they can contribute to radiation hardening of the matrix. When helium bubbles are formed at grain boundaries they may lead to severe intergranular embrittlement at high temperatures.

High temperature helium embrittlement has been attributed to the diffusional growth of cavities on grain boundaries [60,66–69]. Helium bubbles are stabilized by balancing the applied stress and surface tension, which can be described by [69]:

$$\sigma = \frac{2\gamma}{r}\left[1 - \left(\frac{r_0}{r}\right)^2\right], \tag{18}$$

where γ is the specific surface energy, r the bubble radius, r_0 the initial bubble radius. The critical stress that stabilizes helium bubbles is given by

$$\sigma_{\text{c}} = 0.77\frac{\gamma}{r_0}. \tag{19}$$

If the applied stress is greater than the critical stress, the diffusion-controlled growth rate of stabilized helium bubbles can be described by the Hull–Rimmer model by including the effect of gas pressure, P:

$$\frac{\mathrm{d}r}{\mathrm{d}t} = \frac{\delta D_{\text{gb}}\Omega}{2kTr}\frac{(\sigma + P)}{a}. \tag{20}$$

The rupture time of grain boundary cavitation by helium bubbles is determined by integrating Eq. (20):

$$t_{\text{r}} = \frac{2kT}{\delta D_{\text{gb}}\Omega}\cdot\int_{r_0}^{\frac{a}{2}}\frac{a\mathrm{d}r}{\left(\frac{\sigma}{r} + \frac{P}{r}\right)}. \tag{21}$$

The quantities included in the integral in Eq. (21), namely, r, a and P are dependent on the He production rate, irradiation temperature and the microstructure of grain boundaries [66–68] and they are difficult to be determined precisely. Two extreme cases are analyzed here: in the first scenario, the number of helium atoms is fixed in a cavity once the cavity is stabilized. This would represent the case of a high temperature excursion in neutron irradiated material with a constant applied stress. In this case, the gas pressure in the cavity is given by

$$P = \frac{2\gamma\cdot r_0^2}{r^3}. \tag{22}$$

Note that the internal pressure, P drops quickly as a gas bubble grows. The effect of helium pressure on the rupture time is insignificant. In the second scenario, the helium pressure is constant prior to failure, or in other words, there is sufficient helium supply to cavities during the growth stage. Assume that $P \approx P(a/2)$, the rupture time is given by

$$t_{\text{r}} = A\cdot\frac{kTa^3}{(D_{\text{gb}}\delta)\Omega}\cdot\frac{1}{\left(\sigma + \frac{2\gamma}{a}\right)}. \tag{23}$$

4.3. Fracture mechanism maps for irradiated metals and alloys

Fig. 7 shows the irradiation-modified fracture mechanism map of 316 SS. Neutron irradiation increases the yield stress of 316 SS significantly. The yield stress data of neutron-irradiated 316 SS over a dose range of 3–20 dpa are shown in Fig. 7 [70]. It is seen that the yield stress approaches the

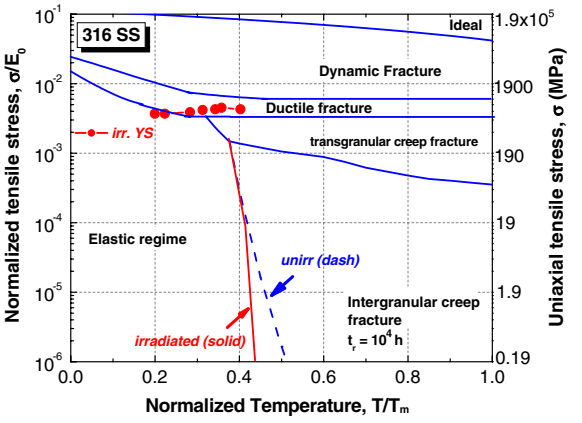

Fig. 7. Calculated fracture mechanism map for irradiated 316 SS (grain size of 50 μm).

plastic instability stress (true ultimate tensile strength) after irradiation due to loss of strain hardening capacity. The plastic instability stress of 316 SS is believed to be unaffected by neutron irradiation before plastic instability at yield takes place [71–74], and therefore the ductile fracture field is not changed by irradiation. However, a new fracture mechanism, 'channel fracture' may come into play when the yield stress is increased to be the same as the plastic instability stress and the onset of plastic instability occurs at the yield point [60]. The 'channel fracture' has been reported mainly in stainless steels irradiated to high doses [75–77]. The mechanism of 'channel fracture' will be included in future work. Fig. 7 also shows the effect of helium on intergranular fracture at high temperature in irradiated 316 SS. The rupture time was determined by Eq. (23) with the assumption of constant helium pressure and constant void spacing (1 μm). It is illustrated in Fig. 7 that the intergranular creep fracture is enhanced by the helium effect, and this helium embrittlement phenomenon can be conveniently included in the fracture mechanism map. It must be pointed out that the model described by Eq. (23) represents a great simplification of the helium effect. The void spacing, which is assumed to be constant, should depend on helium production and diffusion, temperature and material microstructure.

The fracture mechanism map of irradiated Mo is shown in Fig. 8. Fig. 8 gives an example of the effect of radiation hardening on cleavage fracture in neutron-irradiated Mo. The average increase in yield stress in Mo is about 300 MPa after neutron irradiation to a dose of ~1 dpa [47,50]. Due to the increase in the yield stress, the cleavage fracture field is enlarged after irradiation, and the transition temperature from brittle to ductile fracture shifted from $0.09T_m$ to $0.14T_m$. It is apparent that plastic instability at yield occurs during the transition of cleavage to ductile fracture when the yield stress of irradiated Mo is lower than the cleavage stress but is the same as the plastic instability stress. The helium embrittlement at high temperature in irradiated Mo is also illustrated in Fig. 8.

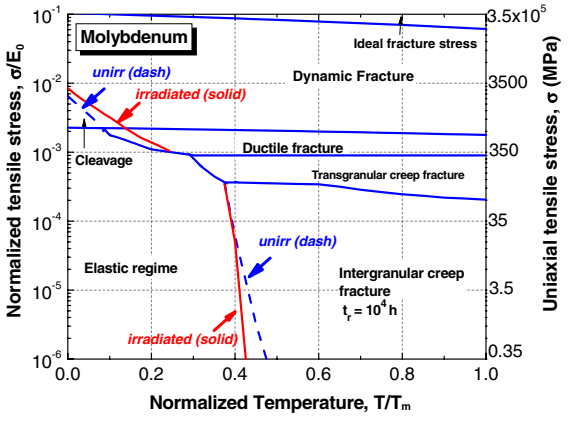

Fig. 8. Calculated fracture mechanism map for irradiated Mo (grain size of 70 μm).

5. Discussion

As a first step to calculate fracture mechanism maps, we simplified the problem by considering only uniaxial tensile loading and excluding stress state and notch effects. The essential physical features in fracture mechanisms were of primary interest. The models that were selected for each fracture mechanism give the simplest form of a constitutive equation. The efforts are intended, at this stage, to illustrate the method of computing fracture mechanism maps and stimulate further research in constructing more detailed and accurate maps. Therefore, the quantitative accuracy of the fracture maps presented in this paper is not considered to be reliable. We have demonstrated that fracture mechanism maps can be computed to give an overview of fracture behavior in response to stress, temperature and neutron irradiation. From a comparison of the calculated maps with empirical fracture maps in the literature, the characteristics of fracture behavior appear to be well represented in the computed maps. For instance, both calculated and observed maps of Mo [10] show cleavage fracture at temperatures below $\sim 0.1T_m$ at normalized stresses, σ/E_0 less than 0.01. As temperature increases the fracture mode changes to ductile fracture. It was also shown in both maps that creep fracture starts above $0.3T_m$ in Mo, with transgranular creep fracture dominant at high stresses and intergranular creep fracture dominant at low stresses and high temperatures. A good agreement was also seen in the calculated and observed fracture mechanism maps for 316 SS. Additionally, it was noted that metals and alloys with the same crystal structure have similar fracture mechanism maps. The maps for fcc metals show five principal mechanism-fields: fracture at the ideal strength, dynamic fracture, low temperature ductile fracture, transgranular creep fracture and intergranular creep fracture. Cleavage fracture is not observed in fcc materials, which differentiates them

from bcc metals and alloys. Among bcc metals the tendency to cleavage fracture is different: Mo has the greater tendency for cleavage fracture than V4Cr4Ti. Experimentally, this trend is observed in all Group V versus Group VI metals [49,73].

In this preliminary study, we have found many questions that remain unanswered and many variations remain to be explored. Listed below are several areas that are required for future exploration.

It was mentioned in the previous section that the material property data used in the constitutive equations are mostly textbook values. More accurate maps could be generated if material parameters such as diffusion coefficients for lattice, grain boundary and dislocation core diffusion and dislocation creep parameters are derived by fitting the constitutive equations to experimental fracture data of the material. In the previous work by Ashby and others, the empirical fracture mechanism maps were constructed by assembling the tensile and creep data of un-notched round bar specimens, and by observation of fractographic appearance. The ultimate tensile strength data from tensile tests were chosen for the fracture strength at low temperatures, and the creep fracture data were obtained from constant-load creep tests. Although there are ambiguities and difficulties in obtaining proper fracture data from experiments, and there are concerns about impurities, grain size variations, etc., the parameters shown in the constitutive equations can and should be adjusted from experimental data to give the best description of material fracture response.

The calculated fracture maps are not complete in terms of fracture mechanisms considered. In the fracture mechanism maps constructed by Gandhi and Ashby [9,10], three types of cleavage fracture were classified. Cleavage I refers to the fracture that occurs from a pre-existing flaw without any general plasticity; cleavage II is a brittle fracture from a crack nucleated by slip or twinning below general yielding; cleavage III refers to a cleavage fracture after general yielding with measurable plasticity. These subdivisions of cleavage fracture were not considered in the calculated maps. The fracture stress of cleavage fracture in the calculated maps was defined by microcrack nucleation by slip only. Brittle intergranular fracture at low temperature that is observed in many high-strength bcc metals and alloys, particularly those prepared by powder metallurgy techniques, was also not included in the calculated maps. In addition, it is possible to subdivide the intergranular creep fracture field into a regime at lower stresses where spherical voids grow on grain boundaries and a regime at higher stress where wedge-like cracks at triple-points are dominant. Rupture and dynamic recrystallization should also be included in future calculations.

One of the most complicated issues in constructing fracture mechanism maps is perhaps the dependence of fracture processes on specimen geometry and dimensions and the notch sensitivity. Due to constraint effects in fracture, specimen geometry and dimensions are important. Flat specimens tend to fail by rupture more readily than round bar specimens because unconstrained necking leads to rapid thinning through the thickness of the flat plate. The reduced constraint also means that the fracture stress will be lower. Necking is another issue that needs to be considered in fracture studies. The total fracture strain is composed of uniform elongation and elongation due to necking. The necking strain will be dependent on specimen size and shape [19]. The introduction of a notch will significantly change the fracture process as well. A notch produces a high local stress and a high localized strain and creates a triaxial stress state. The tendency for brittle fracture is therefore increased in a notched specimen. The effect of hydrostatic pressure on tensile fracture strain is also significant. It was suggested the stress intensity factor (instead of tensile stress) may be a more appropriate parameter in fracture mechanism maps [78].

Fracture behavior is far more complex than plastic deformation behavior. Constitutive modeling of fracture mechanisms is still in a developing stage. The maps shown here are based on the simplest equations derived from the physical models of fracture mechanisms. More precise models are needed in future efforts. For example, the grain boundary cavitation at high temperatures is always limited by flow of the surrounding matrix. The Hull–Rimmer model that was employed in this study represents the unconstrained cavity growth process. In reality, creep flow has to play an important role in the fracture process, and therefore a constrained cavity growth model is more appropriate for modeling such a physical process. For low temperature ductile fracture by void nucleation, growth and coalescence, there are practically no reliable physical models that can be used to predict the true fracture stress.

Regarding the irradiation effects on the fracture processes in metals and alloys, cleavage fracture at

low temperatures and helium embrittlement at high temperature are two of the most detrimental issues in nuclear reactor design. There has been a vast amount of effort in modeling helium effects on grain boundary cavitation. What has been discussed in this paper was a simplified model that should be considered for the purpose of illustrating the modification of fracture mechanism maps only. More detailed and comprehensive information on high temperature helium embrittlement can be found in the papers by Trinkaus et al. [66–68,79], although these models are not easily adapted to derive constitutive equations for fracture. It should also be emphasized that 'channel fracture' [60,69,75–77] is unique in irradiated metals and alloys. The inclusion of dislocation channeling in deformation mechanism maps and channel fracture mode in fracture mechanism maps for irradiated metals and alloys is of high interest for nuclear structural material applications, and it should be given increased attention in future studies.

Due to the lack of suitably accurate constitutive equations, fracture mechanism maps are more difficult to construct and less quantitative than deformation mechanism maps. Nevertheless, they give an overview of the micromechanisms by which a given material may fail, and help identify the mechanism most likely to be dominant in a given experiment or an engineering application. They can give guidance in selecting materials for high temperature use, and in the extrapolation of creep-rupture data. When used appropriately, they can have profound impact on understanding the fracture processes of irradiated materials and they will help in the prediction of the fracture behavior of engineering materials in irradiated conditions.

6. Conclusions

A theoretical framework of calculating fracture mechanism maps is introduced. Several basic fracture mechanisms are described by physically-based constitutive equations that define stress-temperature fields in fracture mechanism maps. The calculated fracture mechanism maps of reactor engineering materials such as CuCrZr, 316 SS, Mo, F82H and V4Cr4Ti represent well the observed fracture characteristics and dominance of mechanisms at a given stress and temperature condition. The maps also show changes in fracture processes after irradiation: radiation-induced hardening expands the regime of cleavage fracture of bcc metals, and high temperature helium embrittlement significantly modifies the intergranular creep fracture regime. The concept of fracture mechanism maps has shown its usefulness in identifying dominant fracture mechanisms and in categorizing some important radiation effects on the fracture behavior of engineering materials.

Acknowledgements

The research was sponsored by the Office of Fusion Energy Sciences, the US Department of Energy under contract DE-AC05-00OR22725 with Oak Ridge National Laboratory, managed and operated by UT-Battelle, LLC. The authors would like to thank Mr J. Merkle for his valuable input. The authors would also like to thank Drs M. Sokolov and R. Nanstad for their technical reviews.

References

[1] M.S. Wechsler, The Inhomogeneity of Plastic Deformation, Am. Society for Metals, Metals Park, OH, 1972, p. 19.
[2] M.S. Wechsler, The Interaction of Radiation with Solids, North-Holland, Amsterdam, 1964, p. 246.
[3] M.F. Ashby, Acta Metall. 20 (1972) 887.
[4] H.J. Frost, M.F. Ashby, Deformation-Mechanism Maps: The Plasticity and Creep of Metals and Ceramics, Pergamon, 1982.
[5] S.J. Zinkle, G.E. Lucas, Fusion Materials Semi-annual Progress Reports, DOE/ER-0313/34, 2003, p. 101.
[6] Meimei Li, S.J. Zinkle, J ASTM Int. 2 (2005) 267.
[7] P.J. Wray, J. Appl. Phys. 40 (1969) 4018.
[8] M.F. Ashby, Cambridge University Engineering Department Report, CUED/C/MATS/TR.34, 1977.
[9] M.F. Ashby, C. Gandhi, D.M.R. Taplin, Acta Metall. 27 (1979) 699.
[10] C. Gandhi, M.F. Ashby, Acta Metall. 27 (1979) 1565.
[11] R.J. Fields, T. Weerasooriya, M.F. Ashby, Metall. Trans. A 11A (1980) 333.
[12] G.D. Quinn, J. Mater. Sci. 25 (1990) 4361.
[13] Z. Bin Ahmad, M.F. Ashby, J. Mater. Sci. 23 (1988) 2037.
[14] D. Teirlinck, F. Zok, J.D. Embury, M.F. Ashby, Acta Metall. 36 (1988) 1213.
[15] C. Zener, Tran. ASM 40A (1948) 3.
[16] A.N. Stroh, Proc. R. Soc. A223 (1954) 404.
[17] D.A. Curry, Met. Sci. 14 (1980) 319.
[18] A.H. Cottrell, Tans. AIME 212 (1958) 192.
[19] G.E. Dieter, Mechanical Metallurgy, 2nd Ed., McGraw-Hill Book Company, 1976.
[20] S.H. Goods, L.M. Brown, Acta Metall. 27 (1979) 1.
[21] L.M. Brown, W.M. Stobbs, Philos. Mag. 34 (1976) 351.
[22] J.R. Rice, D.M. Tracy, J. Mech. Phys. Solids 17 (1969) 201.
[23] P.F. Thomason, J. Inst. Met. 96 (1968) 360.
[24] P.F. Thomason, Acta Metall. 29 (1981) 2127.
[25] P.F. Thomason, Acta Metall. 41 (1993) 763.
[26] F.C. Monkman, N.J. Grant, Proc. ASTM 56 (1956) 593.
[27] D. Hull, D.E. Rimmer, Philos. Mag. 4 (1959) 673.
[28] M.V. Speight, J.E. Harris, J. Met. Sci. 1 (1967) 83.

[29] B.F. Dyson, Can. Metall. Quart. 18 (1979) 31.
[30] B.F. Dyson, M.J. Rodgers, J. Met. Sci. 8 (1974) 261.
[31] G.H. Edward, M.F. Ashby, Acta Metall. 27 (1979) 1505.
[32] W.M. Garrison Jr., N.R. Moody, J. Phys. Chem. Solids 48 (1987) 1035.
[33] G. Le Roy, J.D. Embury, G. Edward, M.F. Ashby, Acta Metall. 29 (1981) 1509.
[34] T.S. Byun, N. Hashimoto, K. Farrell, Acta Mater. 52 (2004) 3889.
[35] A.A.F. Tavassoli, J. Nucl. Mater. 258–263 (1998) 85.
[36] G. Kalinin, V. Barabash, A. Cardella, J. Dietz, K. Ioki, R. Matera, R.T. Santoro, R. Tivey, J. Nucl. Mater. 283–287 (2000) 10.
[37] A.D. Ivanov, A.K. Nikolaev, G.M. Kalinin, M.E. Rodin, J. Nucl. Mater. 307–311 (2002) 673.
[38] ASM Handbook, ASM International, Materials Park, OH, 2000.
[39] Aerospace Structural Metals Handbook, CINDAS/USAF CRDA Handbooks Operation, Purdue University, 1999.
[40] Handbook on Materials for Superconducting Machinery, Metals and Ceramics Information Center, Battelle, Columbus, OH, 1977.
[41] D.B. Mann, LNG Materials and Fluids, National Bureau of Standards, Boulder, CO, 1978.
[42] K.G. Brickner, J.D. Defilippi, Handbook of Stainless Steels, McGraw-Hill, New York, 1977.
[43] A. Nyilas, K. Nikbin, A. Portone, C. Sborchia, in: Advances in Cryogenic Engineering, Transactions of the International Cryogenic Materials Conference – ICMC, vol. 48, 2002, p. 165.
[44] G.P. Sanderson, D.J. Llewellyn, J. Iron Steel Inst. 207 (1969) 1129.
[45] L.F. Li, K. Yang, L.J. Rong, in: Advances in Cryogenic Engineering, Transactions of the International Cryogenic Materials Conference – ICMC, vol. 50, 2004, p. 176.
[46] R.L. Tobler, A. Nishimura, J. Yamamoto, Cryogenics 37 (1997) 533.
[47] Meimei Li, N. Hashimoto, T.S. Byun, L.L. Snead, S.J. Zinkle, J. Nucl. Mater., in press.
[48] Meimei Li, T.S. Byun, N. Hashimoto, L.L. Snead, S.J. Zinkle, Fusion Materials Semi-annual Progress Reports, DOE/ER-0313/39, 2005, p. 92.
[49] T.E. Tietz, J.W. Wilson, Behavior and Properties of Refractory Metals, Stanford University, Stanford, CA, 1965.
[50] B.V. Cockeram, J.L. Hallenbeck, L.L. Snead, J. Nucl. Mater. 324 (2004) 77.
[51] H.M. Chung, B.A. Loomis, D.L. Smith, J. Nucl. Mater. 239 (1996) 139.
[52] D.L. Smith, M.C. Billone, K. Natesan, Inter. J. Refract. Met. Hard Mater. 18 (2000) 213.
[53] A.N. Gubbi, A.F. Rowcliffe, W.S. Eatherly, L.T. Gibson, Fusion Materials Semi-annual Progress Reports, DOE/ER-0313/20, 1996, p. 38.
[54] G.R. Odette, E. Donahue, G.E. Lucas, J.W. Sheckherd, Fusion Materials Semi-annual Progress Reports, DOE/ER-0313/20, 1996, p. 11.
[55] D.T. Hoelzer, A.F. Rowcliffe, J. Nucl. Mater. 307–311 (2002) 596.
[56] E.V. van Osch, M.I. de Vries, J. Nucl. Mater. 271&272 (1999) 162.
[57] S.J. Zinkle, J.P. Robertson, R.L. Klueh, Fusion Materials Semi-annual Progress Reports, DOE/ER-0313/24, 1998, p. 135.
[58] A.A.F. Tavassoli, J.W. Rensman, M. Schirra, K. Shiba, Fus. Eng. Des. 61&62 (2002) 617.
[59] A.F. Rowcliffe, J.P. Robertson, R.L. Klueh, K. Shiba, D.J. Alexander, M.L. Grossbeck, S. Jitsukawa, J. Nucl. Mater. 258–263 (1998) 1275.
[60] M.L. Grossbeck, J.O. Stiegler, J.J. Holmes, in: M.L. Bleiberg, J.W. Bennett (Eds.), Radiation Effects in Breeder Reactor Structural Materials, TMS-AIME, New York, 1977, p. 95.
[61] E. Orowan, Rep. Prog. Phys. 12 (1948) 185.
[62] J.F. Knott, Fundamentals of Fracture Mechanics, John Wiley, New York, 1973, p. 180.
[63] J.R. Rice, in: H. Liebowitz (Ed.), Fracture: An Advanced Treatise, vol. 2, Academic Press, New York, 1968, p. 191.
[64] T.S. Byun, N. Hashimoto, K. Farrell, J. Nucl. Mater., in press.
[65] E.V. van Osch, M.G. Horsten, M.I. de Vries, J. Nucl. Mater. 258–263 (1998) 301.
[66] H. Trinkaus, J. Nucl. Mater. 118 (1983) 39.
[67] H. Trinkaus, H. Ullmaier, J. Nucl. Mater. 212–215 (1994) 303.
[68] H. Trinkaus, H. Ullmaier, J. Nucl. Mater. 85&86 (1979) 823.
[69] E.E. Bloom, in: Proceedings of Irradiation Embrittlement and Creep in Fuel Cladding and Core Components, London, November 1972, p. 93.
[70] J.E. Pawel, A.F. Rowcliffe, G.E. Lucas, S.J. Zinkle, J. Nucl. Mater. 239 (1996) 126.
[71] T.S. Byun, K. Farrell, Acta Mater. 52 (2004) 1597.
[72] X. Wu, X. Pan, Meimei Li, J.F. Stubbins, J. ASTM Int. 3 (2006) 185.
[73] X. Wu, X. Pan, Meimei Li, J.F. Stubbins, J. Nucl. Mater. 343 (2005) 302.
[74] S.J. Zinkle, N.M. Ghoniem, Fus. Eng. Des. 51&52 (2000) 55.
[75] C.W. Hunter, R.L. Fish, J.J. Holmes, ANS Trans. 15 (1972) 254.
[76] R.L. Fish, C.W. Hunter, ASTM STP 611 (1976) 119.
[77] F.H. Huang, Inter. J. Fract. 25 (1984) 181.
[78] D.G. Brandon, Scr. Metall. 14 (1980) 55.
[79] S.S. Vagarali, G.R. Odette, J. Nucl. Mater. 103&104 (1981) 1239.